Bulletin of the Seismological Society of America, Vol. 109, No. 5, pp. 1968–1984, October 2019, doi: 10.1785/0120180333

Ⓔ

Upper-Crustal Anisotropy of the Conjugate Strike-Slip Fault Zone in Central Tibet Analyzed Using Local Earthquakes and Shear-Wave Splitting

by Chenglong Wu, Xiaobo Tian,* Tao Xu,* Xiaofeng Liang, Yun Chen, Gaohua Zhu, José Badal, Zhiming Bai, Guiping Yu,† and Jiwen Teng

Abstract Remarkable V-shaped conjugate strike-slip faults extend along the Bangong–Nujiang suture in central Tibet. Motions of these faults are considered to accommodate ongoing east–west extension and north–south contraction. Fabrics within the fault zone that are anisotropic to seismic waves can provide clues as to the unusual scale and style of lithospheric deformation. With the goal of determining the upper-crustal anisotropy pattern in central Tibet, we measured shear-wave splitting parameters (fast wave polarization direction and delay time) using waveforms generated by 194 local earthquakes recorded by 49 stations of the SANDWICH network. Stations located in eastern and western zones of the study area show anisotropy directions that agree well with the maximum horizontal compressive stress direction. The fast polarization directions at stations near active strike-slip faults generally run parallel to the strikes of these faults. Pervasive inactive thrust faults caused by Cretaceous–Tertiary shortening in central Tibet also clearly correlate with the anisotropy detected at nearby stations. These results demonstrate that both local structures and stress contribute to upper-crustal anisotropy in the region. Combining the new results with previous *SKS*-wave splitting results and other seismic evidence, we propose that deformation in the upper crust is mechanically decoupled from that in the upper mantle, due to eastward middle-lower crustal flow. This crustal flow causes basal shearing required for the formation of conjugate strike-slip faults in central Tibet.

Supplemental Content: Tables listing detailed information of the 331 splitting results in this study, centroid moment tensors (CMTs) in the study area from January 1976 to August 2013 from Global CMT project, CMTs from Zhu *et al.* (2017), information of all the 486 earthquake events located by the SANDWICH array, information of the 231 events presented in Zhu *et al.* (2017) from November 2013 to November 2014, information of the 255 events located by subsequent SANDWICH seismic data from November 2014 to October 2015, and the average fast directions of each station, and their closest fast directions of *SKS* splitting along with the strikes of their closest faults, and their angle difference, map of epicenters, and figures showing depth distribution of earthquakes, comparison of moment tensors, and *S*-wave splitting measurements.

Introduction

The Himalayan–Tibet orogeny presents an ongoing opportunity to study complex crustal dynamics of continent–continent convergence. The orogen absorbed at least 1400 km of north–south shortening since the onset of the Indo-Asian collision at about 65 Ma (Yin and Harrison, 2000). Mechanisms responsible for accommodating the shortening remain uncertain despite intensive study. The lateral extrusion model emphasizes the role of large-scale strike-slip faults in transporting relatively undeformed continental blocks away from the convergent front, such that the greatest amount of deformation occurs along the major shear zones (Tapponnier *et al.*, 1982,

*Also at CAS Center for Excellence in Tibetan Plateau Earth Sciences, Beijing 100101, China.

†Also at University of Chinese Academy of Sciences, Beijing 100049, China.

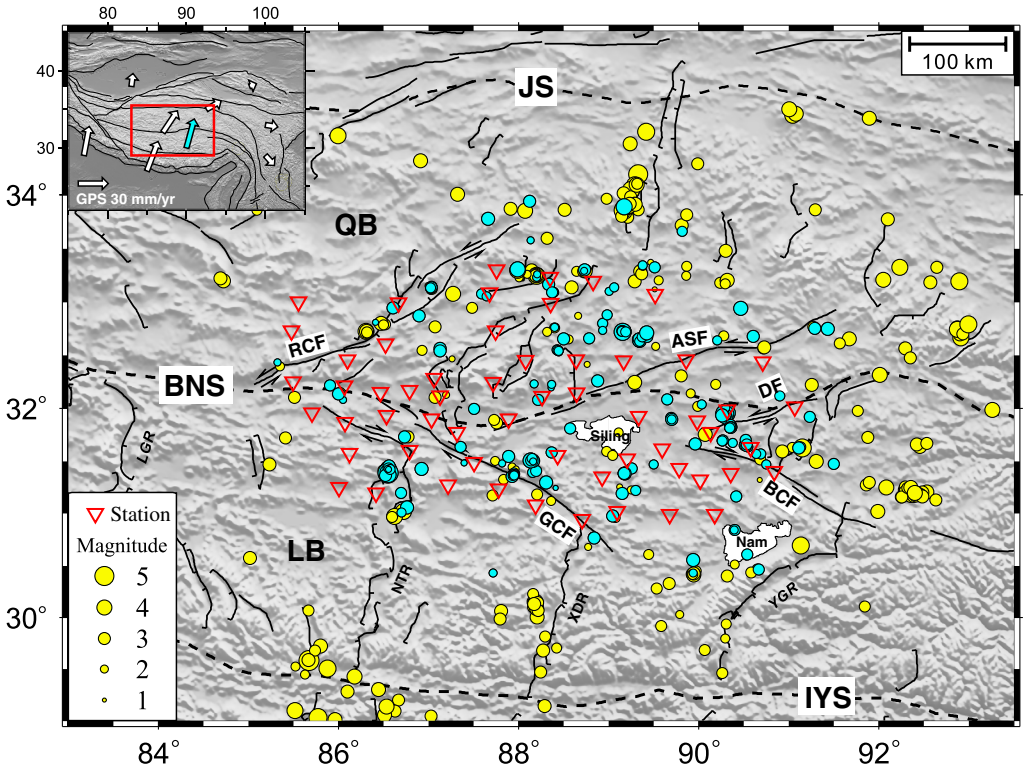

Figure 1. Shaded topographic map showing the main tectonic features in central Tibet, location of the SANDWICH seismic array (inverted red triangles), and epicenters of regional earthquakes (yellow and light blue circles, Zhu *et al.*, 2017). The magnitude scale is given in legends. Seismic events in light blue represent the earthquakes used for shear-wave splitting (SWS) analysis. The study area is contoured by a red rectangle in the inset. White arrows in this inset represent Global Positioning System (GPS) velocities from Gan *et al.* (2007). The blue arrow shows the average stress direction 15.3° ± 6.1° in the study area (see Data and Resources, Ⓔ Table S1, available in the supplemental content to this article). ASF, Amdo-Sewa fault; BCF, Beng Co fault; BNS, Bangong–Nujiang suture; DF, Dongqiao fault; GCF, Gyaring Co fault; IYS, Indus-Yarlung suture; JS, Jinsha suture; LB, Lhasa block; LGR, Longgar rift; Nam, Nam Co; NTR, Nyima-Tingri rift; QB, Qiangtang block; RCF, Riganpei Co fault; Siling, Siling Co; XDR, Xainza-Dingjye rift; YGR, Yadong-Gulu rift. The color version of this figure is available only in the electronic edition.

2001). By contrast, the thin viscous sheet model assumes that the entire Tibetan plateau uniformly shortens and thickens (England and McKenzie, 1982; England and Houseman, 1986) thereby requiring widely distributed deformation throughout the plateau. Growing evidence supports the theory that middle-lower crustal flow inflates the crust to cause the thickening of the crust and uplift of the plateau (Clark and Royden, 2000). Ductile flow separates deformation between the upper-crust and upper-mantle lithosphere. Investigating deformation around major faults can help constrain understanding of mechanisms and present-day kinematics of the Indo-Asian collision.

Global Positioning System (GPS) velocities indicate that north-northeast–south-southwest-trending features and the collisional margin itself are still undergoing horizontal shortening (Wang *et al.*, 2001; Zhang *et al.*, 2004; Gan *et al.*, 2007). Given the intensity of compression, active structures in the interior of the plateau assume a mix of normal and strike-slip deformation (Taylor and Peltzer, 2006). V-shaped conjugate strike-slip faults are significant structures along the Bangong–Nujiang suture (BNS) zone in central Tibet (Taylor *et al.*, 2003). These conjugate faults consist of northeast-striking sinistral faults north of the BNS and northwest-striking dextral faults south of the suture zone (Fig. 1). Motion along these strike-slip faults and associated north-trending rifts along their northern and southern flanks accommodate coeval east–west extension and north–south contraction of the plateau (Taylor *et al.*, 2003). To interpret how conjugate faults form, Yin and Taylor (2011) proposed a paired general-shear model. They suggest that combined effects of synchronous north–south contraction and eastward asthenospheric flow induced paired lithospheric general shear zones that then generated conjugate faults. The paired general-shear model implies that the Tibetan crust deforms contiguously with the underlying mantle lithosphere (for a given vertical section), such that conjugate faults represent lithospheric-scale features (Yin, 2000). However, little is known about crustal anisotropy in central Tibet. This information could help resolve links between crustal deformation and conjugate faults.

Shear-wave splitting (SWS) studies demonstrated that azimuthal seismic anisotropy, defined as the polarization orientation of the fast shear wave (φ) and the splitting delay time (δt) between the fast and slow shear waves, can effectively image deformation in the crust and mantle (Silver and Chan, 1991; Silver, 1996; Savage, 1999). In the upper mantle, anisotropy

is interpreted as lattice preferred orientation (LPO) of intrinsically anisotropic mantle minerals, namely olivine (Zhang and Karato, 1995). Similar to the upper mantle, anisotropy in the middle to lower crust is interpreted to reflect the LPO of anisotropic minerals, including amphibole, biotite, and muscovite (Tatham *et al.*, 2008). Ko and Jung (2015) suggest that channelized plastic flow in the middle to lower crust can result in azimuthal anisotropy with fast polarization directions subparallel to the flow direction. However, anisotropy in the upper crust is interpreted from different mechanisms that fall into two general categories (Boness and Zoback, 2006). One is stress-induced anisotropy caused by alignment of cracks in response to the *in situ* stress field. The fast direction of the vertically propagating shear wave agrees with the maximum horizontal compressive stress direction (hereafter, az$S_{\mathrm{H\,max}}$) (Crampin *et al.*, 1978; Boness and Zoback, 2004; Savage, Ohminato, *et al.*, 2010). The other category is structural anisotropy, which occurs when macroscopic features such as fault-zone fabric, sedimentary bedding planes (Leary *et al.*, 1990), or aligned minerals and/or grains (Kern and Wenk, 1990) polarize *S* waves along a fast direction within planes defined by the feature. Numerous studies considered SWS near active faults in investigating upper-crustal anisotropy (Savage *et al.*, 1989; Aster *et al.*, 1990; Zhang and Schwartz, 1994; Zinke and Zoback, 2000; Tadokoro and Ando, 2002; Cochran *et al.*, 2003, 2006; Boness and Zoback, 2004, 2006; Liu *et al.*, 2004, 2008; Nascimento *et al.*, 2004; Peng and Ben-Zion, 2004, 2005; Gao *et al.*, 2011; Yang *et al.*, 2011; Cochran and Kroll, 2015; Guo *et al.*, 2015; Li *et al.*, 2015; Li and Peng, 2017). Most of these works interpret observed anisotropy as arising from a combination of regional stress and shear fabrics within the fault. For example, Cochran *et al.* (2006) investigated the anisotropic field along the San Andreas fault and found that fault-parallel measurements span a 150-meter-wide zone of pervasive cracking and damage from fault-zone-trapped waves associated with the main fault core. The fast directions are subparallel to az$S_{\mathrm{H\,max}}$ outside of this zone. Liu *et al.* (2008) and Li *et al.* (2015) also found that both stress and structure controlled anisotropy in the San Andreas fault zone and nearby regions at different scales. Applying the TESSA 2D δt-tomography and φ-spatial averaging technique, Johnson *et al.* (2011) and Cochran and Kroll (2015) similarly found a mixture of fast directions oriented generally parallel to az$S_{\mathrm{H\,max}}$ or to the strikes of faults around the Mount Ruapehu volcano of New Zealand, and around the Yuha Desert of California.

During the last two decades, a number of SWS studies have been carried out around central Tibet (Sandvol *et al.*, 1997; Chen and Ozalaybey, 1998; Huang *et al.*, 2000; Fu *et al.*, 2008; Chen, Martin, *et al.*, 2010; Zhao *et al.*, 2014; Chen *et al.*, 2015; Wu *et al.*, 2019). Most of these focused on *SKS* splitting, which captures upper-mantle anisotropy and typically neglects contributions from crustal anisotropy. Most fast polarization directions detected by previous studies strike in an east-northeast–west-southwest direction. To determine crustal deformation, some studies performed splitting analysis of Moho-converted *Pms* waves previously extracted from teleseismic *P*-wave receiver functions in Tibet (Sun *et al.*, 2012; Wu *et al.*, 2015; Wang *et al.*, 2016). The *Pms*-delay times from 16 stations are greater than 0.5 s. The strong anisotropy detected implies that many parts of the Tibetan crust have undergone major deformation related to crustal flow. SWS analysis applied to *S* waves generated by local earthquakes can effectively estimate upper-crustal anisotropy and provide clues about crustal deformation. Few studies used this approach in central Tibet. To fill this gap, we applied SWS analysis to local earthquakes recorded by stations in the SANDWICH seismic network that specifically cover conjugate faults zones in central Tibet. Similar to Savage *et al.* (2016), we then performed stress inversion of earthquake focal mechanisms to compare the stress direction to upper-crustal anisotropy. Finally, we compared results to surface geological observations to interpret the deformation style and mechanisms forming conjugate faults in central Tibet.

Data and Method

The SANDWICH experiment is a 2D broadband seismic array in central Tibet with stations deployed on both sides of the BNS, from the northern Lhasa block to the southern Qiangtang block (Fig. 1). This network included 58 seismograph stations with an average spacing of 40 km operated from November 2013 to April 2016. Each of the stations was equipped with a Güralp CMG-3ESP three-component sensor operating at 50 Hz–30/60 s and a RefTek 72A-8/130-1 digital recorder (Liang *et al.*, 2016). Zhu *et al.* (2017) and subsequent work produced a catalog of local earthquakes from the data collected over the array's operational lifetime. The catalog contains a total of 486 earthquakes with local magnitudes ranging from 1.0 to 5.3 (Fig. 1).

After manually picking *S* waves, we calculated fast polarization directions and delay times of split waves using the MFAST automated software package (Savage, Wessel, *et al.*, 2010). This package determines splitting parameters using the following steps. First, a predefined set of 14 band-pass filters is tested for each event to select the best filter based on signal-to-noise ratio (SNR) criterion and filter width. Second, the method performs automated cluster analysis of a large number of window configurations to determine the most stable solution. Finally, the software assigns quality estimates (A–D) to measurements according to classification of the cluster, SNR, and uncertainty. Special attention is given to recognizing null measurements that may occur when there is no anisotropy in the plane of *S*-wave particle motion or when the initial shear wave is polarized along the fast or slow orientation of the medium (Wüstefeld and Bokelmann, 2007). The MFAST code considers null measurements if fast polarization directions fall within a range of 20° with respect to the incoming polarization or its perpendicular dimension.

Sedimentary layers such as those found in the Qiangtang and Lunpola basins exhibit low-seismic velocity and thus may generate near-vertical ray-path arrivals (Zhou *et al.*, 2019). We

therefore did not use a strict "shear-wave window" criterion (Booth and Crampin, 1985) because this practice could unnecessarily reject too many events (Savage, Wessel, *et al.*, 2010). Instead, we selected events with epicentral distances less than 100 km to avoid excessive refraction or reflection in the seismograms. From this basis, we considered the quality of *S*-wave arrivals and the grading scheme to evaluate MFAST results. The conditions that must be met include: (1) an A or B cluster grade (in agreement with criteria described by Savage, Wessel, *et al.*, 2010), (2) SNR > 3, (3) delay time $\delta t < 0.4$ s and error in the fast polarization direction $\varphi < 25°$, and (4) $20° < |\varphi - S_{pol}| < 70°$, in which S_{pol} is the incoming *S*-wave polarization. Similar studies used these criteria (Peng and Ben-Zion, 2004; Savage, Wessel, *et al.*, 2010). Figure 2 illustrates the procedure using data from a sample event. This method identified a total of 331 splitting measurements that met the criteria described earlier from 194 earthquakes. All events occurred in the upper 30 km of the crust, and most were shallower than 20 km, such that they were likely influenced by seismic anisotropy in the upper crust.

To compare seismic anisotropy to stress field, we estimated the orientation of the principal stress axes σ_{1-3} of the stress tensor along with the stress ratio $R = (\sigma_1 - \sigma_2)/(\sigma_1 - \sigma_3)$ from the focal mechanism data. All focal mechanisms used here were waveform inversion solutions computed by the Computer Programs in Seismology method (Zhu *et al.*, 2017) or collected from the Global Centroid Moment Tensor database spanning the last 40 yr. We used the MSATSI software package to apply a damped inversion of the stress field in each subregion (Martínez-Garzón *et al.*, 2014). Although absolute magnitudes of principal stresses cannot be obtained using focal mechanism inversions, the stress ratio *R* provides constraints on the relative magnitudes of the three principal stresses, such that $R < 0.5$ or $R > 0.5$ indicate respective transtensional or transpressional regimes. To compare to fast polarization directions, we calculated $\mathrm{az}S_{H\,max}$ (Lund and Townend, 2007) according to the orientation of the principal stress axes in 3D.

Results

Given the distribution of seismicity and focal mechanisms, we divided the study region into three geographical areas (Fig. 3a) for stress-field inversion: the western conjugate strike-slip fault zone (WCS), the eastern conjugate strike-slip fault zone (ECS), and the southern Lhasa block (SL). Figure 3b–d shows the results with scattered clouds of bootstrap-resampled solutions (Ⓔ Table S2, available in the supplemental content to this article). Variation in the stress field exhibits similar tendencies. The σ_3 term presents similar strikes of N90°E and horizontal dips. The σ_1 and σ_2 terms, meanwhile, present strikes approximating a north–south direction and contrasting dips. The stress σ_1 for the SL exhibits vertical dip likely caused by normal-fault mechanisms of several north–south-trending rifts. The σ_1 and σ_2 stresses do not show concentrated bootstrap solutions for the ECS and WCS. The stress ratio *R* is smaller (indicating that the magnitude of σ_2 approaches that of σ_1), implying a combination of normal and strike-slip faults in the region. The average estimate of $\mathrm{az}S_{H\,max}$ from the three areas ($10.0° \pm 12.7°$) approximates north–south direction, reflecting the general orientation of the ongoing Indo-Asian collision.

Given that Moho depth exceeds 60 km in or near central Tibet (Kind *et al.*, 2002; Zhang and Klemperer, 2005; Chen, Badal, and Hu, 2010; Liu *et al.*, 2014; Zhang *et al.*, 2014; Tian *et al.*, 2015) and given that most focal depths for the selected local earthquakes do not exceed 20 km, splitting parameters estimated here primarily characterize deformation in the upper crust. Our results include 331 high-quality pairs of splitting measurements obtained from 194 local events (with local magnitudes from 1.4 to 5.3) recorded at 49 stations (Ⓔ Table S3). Table 1 lists average SWS measurements from all stations, including the four stations, LADO, NWMQ, NZOC, and YARO, that each returned only a single measurement. Figure 4a shows the average fast polarization directions scaled by the mean delay times at SANDWICH stations, along with rose diagrams of fast directions for the split wave (Fig. 4b). Mean delay times range from 0.04 ± 0.10 s to 0.29 ± 0.03 s, with an average value of 0.15 ± 0.01 s. To statistically analyze the parameter φ, we doubled each angle and then calculated the average angle φ and the mean resultant length *R* (Rayleigh test). This quantifies variance in the fast polarization directions as values between 0 and 1 to indicate scattering or clustering, respectively (Cochran *et al.*, 2003). Most stations gave generally consistent fast directions, but Stations NM10 and CZLM gave relatively low *R*-values, which indicate scattered fast directions. Because there are few measurements at some stations, we grouped stations by their locations or distance from faults to derive results having adequate statistical significance (Fig. 5). Stations BALN, DOMA, XEDE, BXCZ, and CZLM are all less than 20 km from the Amdo-Sewa fault. This group is therefore referred to as the ASF. Stations SEZA, XAGO, SEYA, NM10, and ASUO are close to the Gyaring Co fault and a small dextral fault nearby. This group is referred to as the GCF. The other stations are divided into five groups according to location (see Ⓔ Table S4). Fast directions for the seven groups vary considerably, indicating a complex pattern of anisotropy and attendant structural complexity.

Discussion

The Primary Source of Upper-Crustal Anisotropy

Crustal anisotropy is usually interpreted as the preferential opening of fluid-filled cracks under maximum horizontal compressive stress, a process known as stress-induced anisotropy (Crampin *et al.*, 1978; Leary *et al.*, 1990). As shown in Figure 5, the average fast-wave polarization directions at groups WEST and EAST statistically resemble $\mathrm{az}S_{H\,max}$. Although these stations occur within the same stress field, fast directions for some stations, such as NWMQ and WQAM, run parallel to $\mathrm{az}S_{H\,max}$. The MAQN fast direction

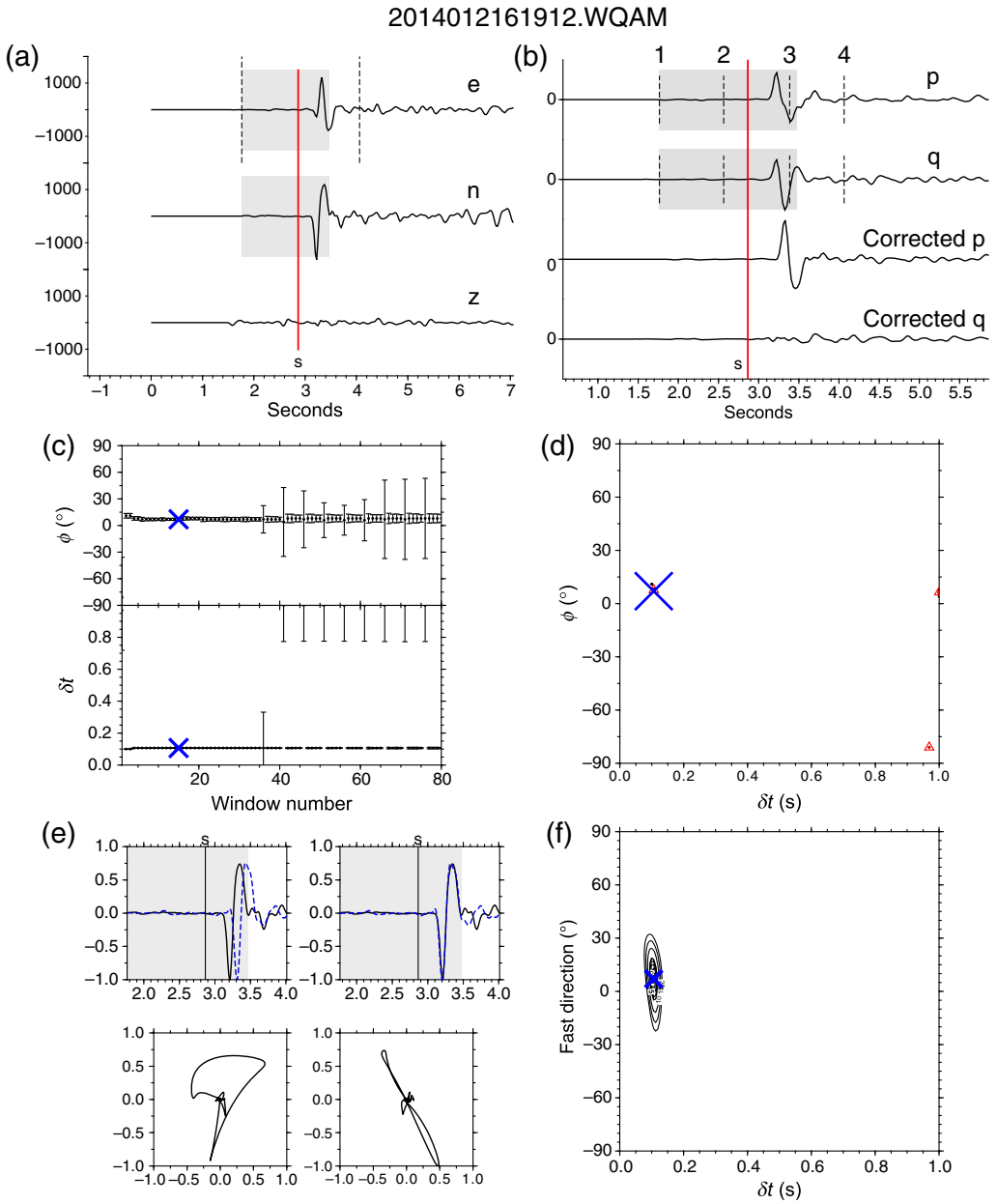

Figure 2. An example of automatic SWS analysis from the signals recorded at Station WQAM that were generated by event 2014012161912 of magnitude 2.8. (a) East–west (e), north–south (n), and vertical (z) displacement components of the 0.2–3.0 Hz filtered waveform. The red line marks the *S* pick. Vertical dashed lines and the gray shading delimit the time window used for SWS analysis. (b) Rotated components to incoming polarization parallel direction (p) and perpendicular direction (q). The two lower components are those corrected for delay time and fast-wave polarization direction. Dashed lines mark the possible range for the start (1 and 2) and end (3 and 4) of the time window. (c) Fast directions (top) and delay times (bottom) determined from 80 different time windows. (d) Distribution of fast directions and delay times determined from different time windows. The blue cross marks the best cluster based on the criteria outlined in Teanby *et al.*, (2004). (e) Waveforms (top row) and particle motions (bottom row) for the original (left column) and SWS-corrected (right column) waveforms. (f) Contours of the second eigenvalue of the covariance matrix for different fast directions and delay times. The blue cross indicates the best-fitting parameters (fast direction $\varphi = 7°$, delay time $\delta t = 0.11$ s). The color version of this figure is available only in the electronic edition.

runs perpendicular to az$S_{H\,max}$. A stress field acting on the crust will align cracks to generate fast directions parallel to the maximum horizontal stress. The same stress field aligns fast directions of anisotropic minerals in a direction parallel to minimum horizontal strain. These effects generate perpendicular fast directions for the two regions. The other five groups show scattered fast directions that differ from az$S_{H\,max}$, with an average misfit angle of 55°. This suggests that, unlike what stress-induced anisotropy implies, the upper-crustal anisotropy does not depend primarily on crustal stress.

Structural anisotropy can also generate a unique seismic response (Boness and Zoback, 2006). The conjugate strike-slip fault system is a prominent and salient geological feature of central Tibet. The observation of strain along these faults

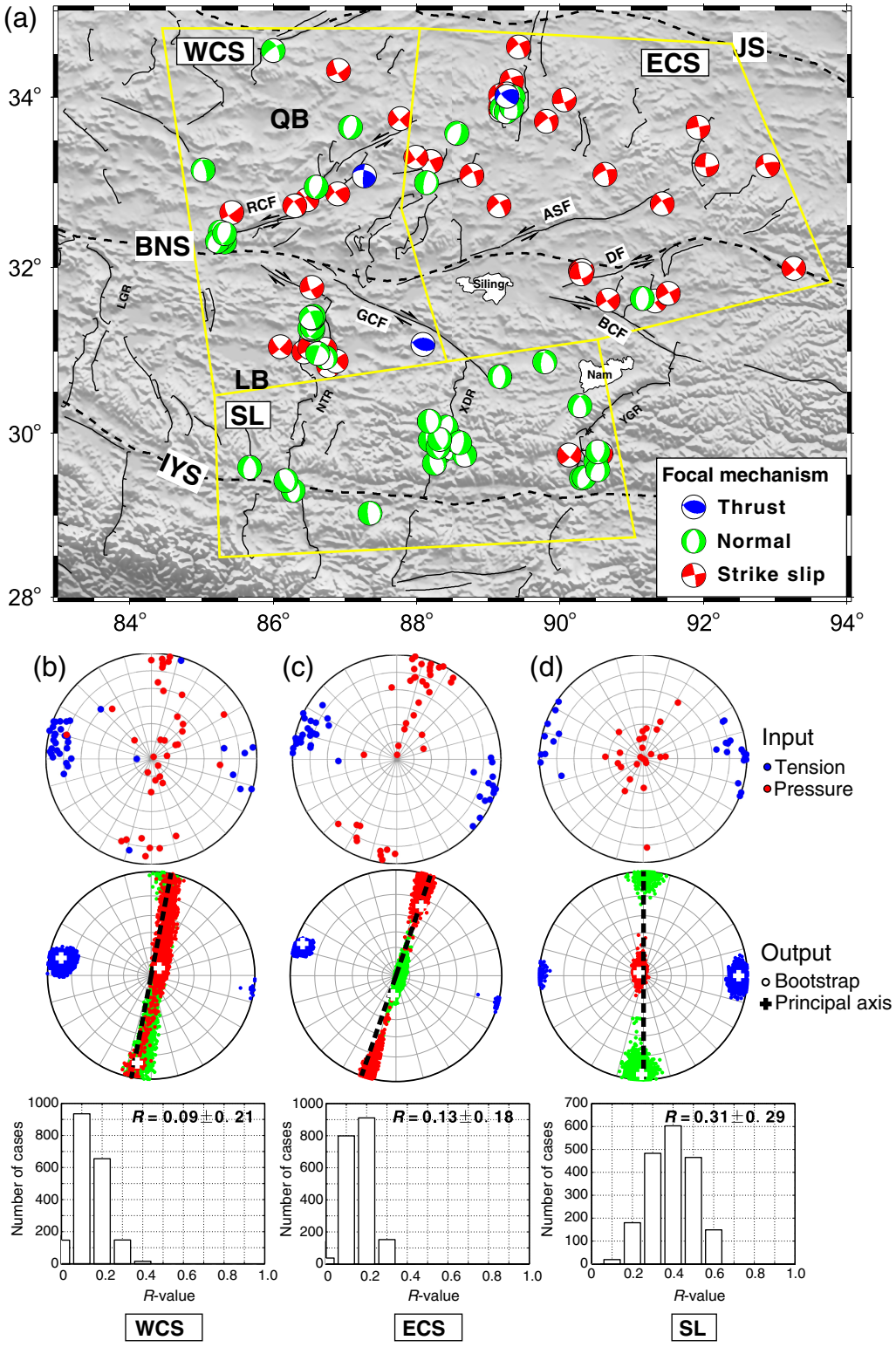

Figure 3. (a) Earthquake focal mechanisms in the study region extracted from the Global Centroid Moment Tensor database (last 40 yr, bottom right corner) and Zhu *et al.* (2017). They have been distributed geographically in three geographical areas (delimited by yellow lines), namely: the western part (WCS), the eastern part (ECS) of the conjugate strike-slip fault zone, and the southern Lhasa block (SL); plots (b–d) refer to these three areas. (b–d) Top panels: principal axes of focal mechanisms in a Schmidt stereo net, used as input for stress-field inversion. Middle panels: inverted stress tensors plotted with principal stress axes (white crosses). Colored circles indicate results of bootstrap inversions. The black dashed line represents maximum horizontal compressive-stress direction. Bottom panels: distribution of the *R*-value for each part. Stress inversion results are shown in Ⓔ Table S2. Abbreviations are the same as in Figure 1. The color version of this figure is available only in the electronic edition.

Table 1
Average Shear-Wave Splitting (SWS) Results for Each Station

Station Code	Latitude (°N)	Longitude (°E)	Elevation (m)	Number of Events	φ (°)	φ_{err} (°)	δt (s)	δt_{err} (s)	*R*-Value
ASUO	31.87	86.07	4812	3	100	12	0.29	0.03	0.77
BALN	32.46	89.86	4691	6	51	16	0.17	0.04	0.48
BAOJ	30.99	90.18	4788	7	139	11	0.16	0.03	0.63
BELA	31.40	90.84	4597	6	105	14	0.18	0.04	0.55
BXCZ	32.11	88.26	4629	8	69	19	0.08	0.01	0.37
CZLM	31.90	87.89	4513	8	70	23	0.15	0.03	0.31
CZQM	33.30	87.76	5000	6	123	25	0.14	0.04	0.32
DENL	32.61	86.52	4751	6	165	10	0.19	0.03	0.68
DOMA	32.45	89.17	4692	24	71	5	0.09	0.01	0.67
EJU1	31.90	87.04	4498	4	61	22	0.18	0.05	0.43
EJU2	31.93	86.53	4705	8	13	11	0.10	0.02	0.58
EJU3	32.15	86.47	4485	9	22	6	0.15	0.01	0.82
ESEL	31.93	89.33	4613	2	75	3	0.16	0.01	0.99
ESUH	33.08	89.52	5069	9	127	4	0.15	0.02	0.92
GACO	33.23	88.35	4806	5	155	12	0.11	0.03	0.65
JAQO	31.63	90.58	4776	23	165	7	0.14	0.02	0.53
LADO	31.20	86.42	4715	1	37	23	0.04	0.10	—
LQLK	31.52	89.20	4602	3	45	15	0.13	0.04	0.67
MABA	31.02	89.09	4681	3	7	17	0.20	0.05	0.61
MAQN	31.78	90.13	4742	5	105	17	0.18	0.03	0.49
MAYU	31.56	88.43	4710	11	62	12	0.10	0.01	0.47
MEDN	31.43	89.78	4613	10	22	9	0.15	0.03	0.65
NIMA	31.77	87.32	4622	3	68	20	0.24	0.02	0.53
NM06	31.27	87.22	4791	13	43	8	0.21	0.03	0.61
NM10	31.49	87.51	4649	12	12	29	0.09	0.01	0.20
NMZ4	32.12	87.13	4761	3	54	6	0.14	0.02	0.94
NMZ6	32.28	87.06	5034	3	97	14	0.09	0.00	0.70
NNRM	32.46	88.08	4746	6	18	12	0.14	0.02	0.63
NWMQ	31.88	89.98	4655	1	32	8	0.21	0.01	—
NXED	32.46	88.64	4621	5	98	9	0.16	0.03	0.77
NZOC	32.25	85.50	4767	1	12	9	0.08	0.01	—
PADO	32.73	87.75	4776	2	39	1	0.14	0.00	1.00
QANM	32.02	91.07	4624	4	6	26	0.10	0.02	0.38
RONM	32.99	86.67	4606	2	40	22	0.11	0.00	0.59
SBGE	31.32	90.02	4820	4	148	32	0.14	0.03	0.31
SEHU	33.19	88.83	4968	10	155	21	0.13	0.02	0.30
SEYA	31.24	87.78	4688	2	109	32	0.10	0.01	0.42
SEZA	30.94	88.70	4669	3	170	8	0.11	0.01	0.89
SMED	30.99	89.68	4729	5	119	15	0.18	0.03	0.54
WBAG	31.61	89.60	4600	6	159	15	0.21	0.04	0.51
WEBU	31.60	86.79	4502	5	51	15	0.13	0.01	0.55
WQAM	31.99	90.32	4639	19	8	3	0.11	0.01	0.93
WRXQ	32.99	88.35	4961	3	50	17	0.23	0.03	0.61
XAGO	31.08	88.19	4729	9	150	17	0.14	0.03	0.39
XEDE	32.15	88.65	4581	5	89	12	0.10	0.03	0.65
XOME	31.35	88.93	4713	7	76	3	0.16	0.02	0.97
YAMJ	31.39	90.35	4628	16	51	7	0.26	0.03	0.66
YARO	32.21	86.07	4515	1	16	7	0.16	0.01	—
ZAQU	32.44	90.71	4762	14	17	10	0.17	0.03	0.51

φ, average fast polarization direction, in degrees from north; φ_{err}, error of φ, one standard deviation; δt, average delay time in seconds; δt_{err}, error of δt, one standard deviation; *R*-value, mean resultant length that quantifies the variance of fast polarization directions as values between 0 and 1 to indicate scattering or clustering, respectively.

indicates that faulting is the dominant mode of deformation in central Tibet, with seismogenic depths extending down to ~25 km (Taylor and Peltzer, 2006). These faults accommodate the pure shear deformation pattern that presently dominates the kinematics of the Tibetan plateau (Chen *et al.*, 2004). Interferometric Synthetic Aperture Radar results indicate left-lateral slip rates of ~6 mm/yr for the Riganpei Co fault and ASF (Taylor and Peltzer, 2006). The Beng Co fault (BCF) and Dongqiao fault (DF) exhibit slip rates of 1–4 mm/yr (Taylor and Peltzer, 2006; Garthwaite *et al.*, 2013). The dextral GCF is one of the pivotal conjugate faults in the region (Taylor *et al.*, 2003). Some workers estimated a high slip rate of 11–15 mm/yr for the fault (Armijo *et al.*, 1989; Taylor and Peltzer, 2006). Reconstruction of displaced lacustrine

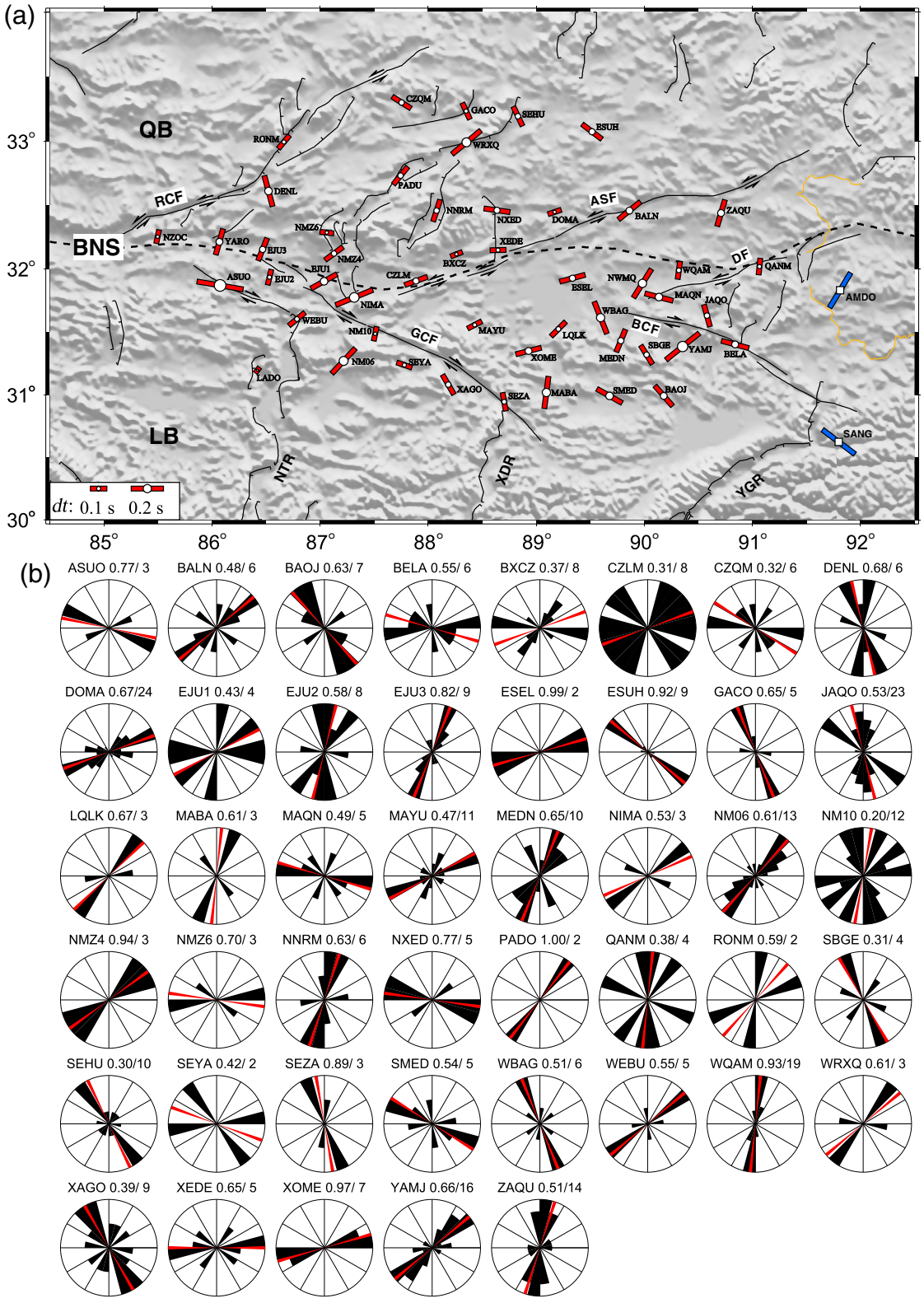

Figure 4. (a) Average SWS vectors (red bars of different length) at SANDWICH stations drawn on a topographic map. Scales for delay times are included in legends. The blue bars represent the upper- to upper-middle-crustal anisotropy (only fast directions) at Stations AMDO and SANG (Sherrington *et al.*, 2004). Abbreviations are the same as in Figure 1. (b) Rose diagrams of fast polarization directions at SANDWICH stations, except for LADO, NWMQ, NZOC, and YARO, which have a single measurement. The numbers included above each rose diagram denote the mean resultant length R-value (see the Results section) and the number of splitting measurements. The red line in each circle represents the average fast polarization direction at the concerned station. The color version of this figure is available only in the electronic edition.

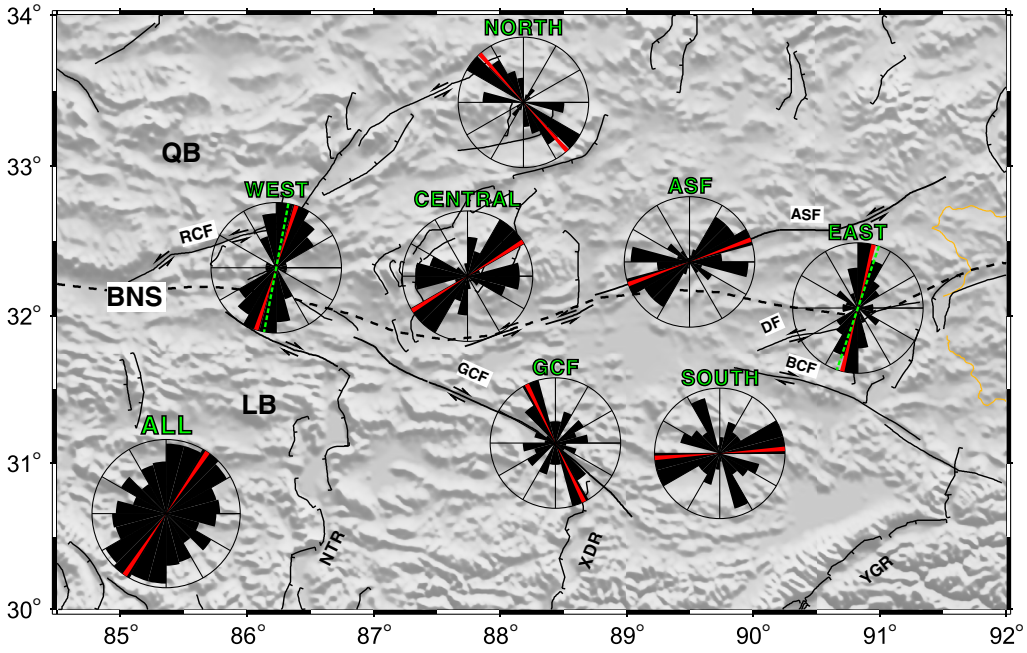

Figure 5. Rose diagrams of fast polarization directions after being grouped for seven different subzones, drawn on a topographic map. The rose diagram with the label ALL (in lower left corner) gathers all estimated directions. The red solid line in each circle represents the average fast direction, and the green dotted line in WEST and EAST represents maximum horizontal compressive-stress direction az$S_{H\,max}$. Abbreviations are the same as in Figure 1. The color version of this figure is available only in the electronic edition.

shorelines across the GCF by Shi *et al.* (2014) gave a slip rate of only 2.2–4.5 mm/yr, however. Conjugate strike-slip faults are active but show varying slip rates that may be reflected in the upper-crustal anisotropy in central Tibet.

Figure 6 shows that fast directions observed from Stations SEZA, XAGO, SEYA near the GCF and Station ASUO near a small dextral fault west of the GCF trend in a northwest–southeast direction consistent with the strikes of the nearby faults. Station NM10 represents an exception, wherein the fast direction approximates az$S_{H\,max}$. Average GCF fast direction orient in a primarily northwest–southeast direction, indicating influence by the northwest-striking GCF fault (Fig. 5). GCF fast directions show some degree of scatter, however. Intersecting faults may lead to different fast directions observed from Stations EJU1 and NIMA near the GCF. As the GCF's conjugate fault, the ASF also apparently influences the anisotropy at nearby stations. Stations CZLM, BXCZ, XEDE, DOMA, and BALN give east-northeast–west-southwest-oriented fast polarization directions generally consistent with the ASF strike (the same as the group ASF in Fig. 5). Fast directions observed from Stations RONM, PADU, NNRM, WRXQ, and LADO run parallel to the strikes of nearby faults and are also consistent with az$S_{H\,max}$, indicating that anisotropy arises from the combined effects of stress and structure. By contrast, fast directions observed from stations near the BCF and DF do not coincide with the strikes of these faults. The BELA station records a fast direction parallel to the BCF strike and thereby represents an exception. Lesser slip rates exhibited by the BCF and DF indicate that these faults are not as active as the GCF and ASF. Consequently, they may exert less influence on fast directions recorded by nearby stations.

Most stations in the NORTH, CENTRAL, and SOUTH groups record fast polarization directions that show little agreement with az$S_{H\,max}$ or with strikes of nearby active faults. Fast directions recorded by CENTRAL and SOUTH groups show considerable variation, indicating other causal factors in producing anisotropy (Fig. 5). Figure 7 shows average fast polarization directions projected onto a tectonic map of the study region (Kapp *et al.*, 2005). Burg *et al.* (1994) suggested that a series of thrust faults related to lithospheric buckling were responsible for initial growth of the Tibetan plateau. Research estimated significant Cretaceous to early Tertiary shortening along these thrust faults within the plateau (Tapponnier *et al.*, 2001; Kapp *et al.*, 2005). Inactivity along these thrust faults for millions of years and other data indicate that shortening has successively stepped out to the margin of the plateau (Tapponnier *et al.*, 2001). Earthquake focal mechanisms, for example, show a combination of strike-slip and normal displacement but seldom show thrusting (Fig. 3). A similar contractional setting, the anticlinorium of the central Qiangtang block, includes upper Paleozoic strata and underlying early Mesozoic mélange. This feature formed by shortening prior to middle Cretaceous volcanism then grew continuously throughout the Tertiary (Kapp *et al.*, 2005). Fast directions from Station CZQM run parallel to the strike of the thrust fault that delimits the anticlinorium to the north. The GACO, SEHU, and ESUH stations located along the plunge of the anticlinorium give northwest–southeast-oriented fast directions potentially related to the feature's internal

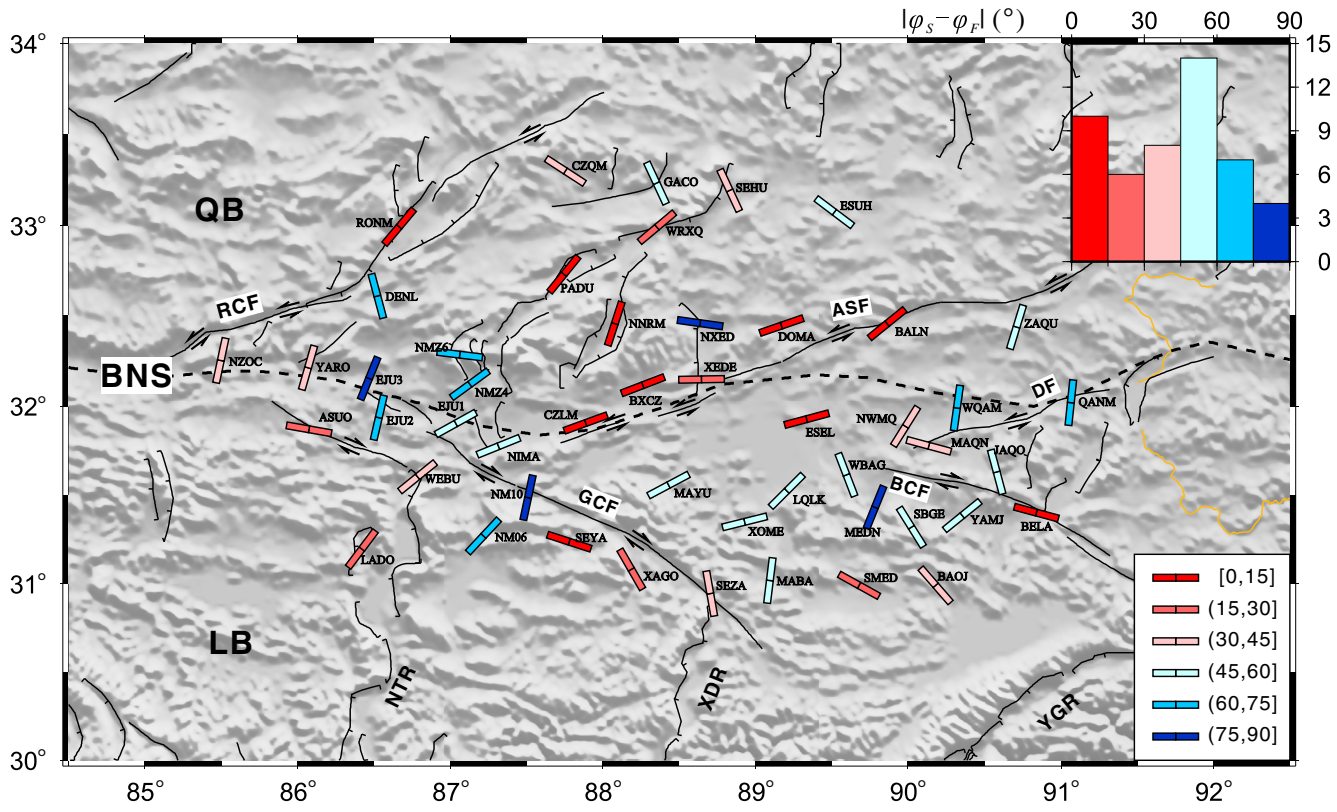

Figure 6. Crustal anisotropy compared with strikes of nearby faults. We use six colors to represent angle difference $|\varphi_S - \varphi_F|$ between fast direction φ_S and the strike of nearby fault φ_F (bottom right corner, in degrees). (Inset) Statistical distribution of aforementioned difference, also with the same colors. The color version of this figure is available only in the electronic edition.

deformation. The approximately east–west-oriented fast directions recorded at Stations NMZ6, NMZ4, and NXED are consistent with nearby north-dipping thrust faults. These cut Eocene–Oligocene red beds and volcanic rocks in their footwall and thereby resemble Paleogene deformation typical of the Qiangtang block (Kapp *et al.*, 2005). Fast directions recorded at ESEL, MAYU, XOME, SMED, and BAOJ agree well with the strikes of the Tertiary south-dipping Gaize-Siling Co backthrust and its southern branch. Heterogeneities in lithological properties (Fig. 7) may cause variations in the fracture response to regional stress and thus cause variation in fast directions recorded by CENTRAL and SOUTH station groups. A similar effect occurs in southern California (Li and Peng, 2017). The complexity of the study area creates complex crustal anisotropy patterns. Future data collection can help resolve sources of variation in fast directions.

Variation in Splitting Parameters with Earthquake Depths

Figure 8 shows delay times for all stations plotted against their event depths. The correlation coefficients for δt and depth is 0.06, indicating a lack of clear dependency of δt on depth. For earthquakes occurring at depths of less than 10 km, 89% of observed delay times (δt) exceed 0.15 s. These results suggest that shallow structures exert obvious influence on upper-crustal anisotropy in this region (Peng and Ben-Zion, 2004; Cochran *et al.*, 2003, 2006; Liu *et al.*, 2004, 2008).

To overcome the limited number of data points and inherent scatter in delay times for a given station, we divided the study area into four zones according to the distribution of seismicity. Each zone is named after the surface structure that concentrates the seismicity (Fig. 9a). The area west of 87.5° E is called the Nyima-Tingri rift zone (NTRZ) because earthquakes occur primarily near the rift. Similarly, the zones between 87.5° and 88.8° E, 88.8° and 90° E, and beyond 90° E are referred to as the Gyaring Co fault zone, Amdo-Sewa fault zone (ASFZ), and Beng Co fault zone, respectively. To explore variation in splitting parameters with focal depths, we projected the splitting parameters along the north–south direction onto event locations and connected them to the corresponding stations (Fig. 9b–e). The spatial distribution of seismicity is complicated but generally relates to subsurface structures of faults observed at the surface. As shown in Figure 9b,c,e, sources in areas with intense seismicity give similar splitting parameters. These observations indicate that near-source properties obviously influence measured anisotropy (Zinke and Zoback, 2000; Cochran and Kroll, 2015).

Figure 10 shows delay times for the four zones plotted versus their event depths. The NTRZ shows a positive correlation between delay time (δt) and event depth, with a correlation coefficient of 0.48. Correlation coefficients for delay

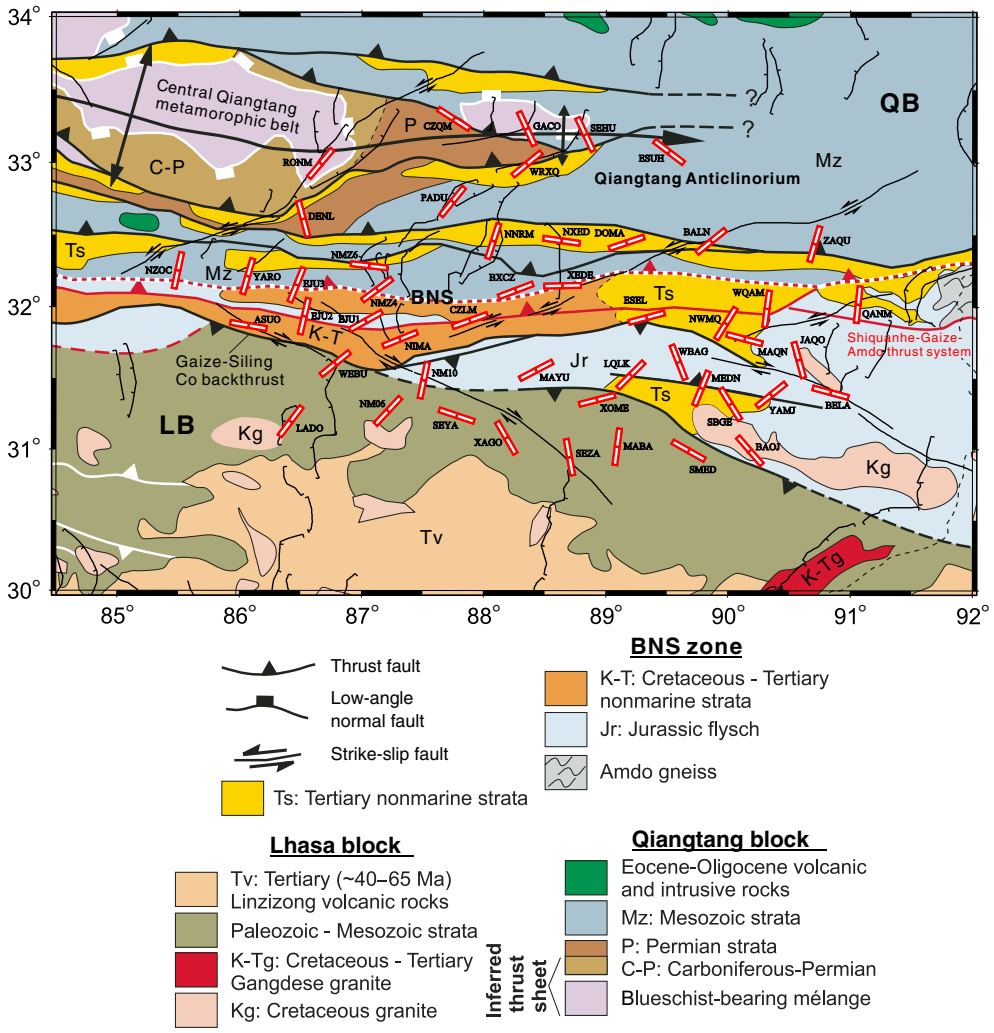

Figure 7. Average fast polarization directions (red open bars) calculated as the circular mean at SANDWICH stations, drawn on a geological map (Kapp, Murphy, *et al.*, 2003; Kapp *et al.*, 2005). Tertiary thrust faults are shown in black. The domal low-angle normal faults of early Mesozoic in the central Qiangtang block are shown in white (Kapp *et al.*, 2000; Kapp, Yin, *et al.*, 2003). Abbreviations are the same as in Figure 1. The color version of this figure is available only in the electronic edition.

time and event depth from other zones were all less than 0.2. The ASFZ gave the smallest average δt-value of 0.13 s (Fig. 10). Low values might arise from ASFZ earthquakes and stations located at some distance from faults.

Deformation Style and Formational Mechanism of Conjugate Strike-Slip Faults in Central Tibet

Matches and mismatches between observations at different depths provide critical clues about geodynamic processes (Chen *et al.*, 2013). Integration of SWS results in central Tibet and surrounding areas with other datasets can help resolve the crust and mantle deformation pattern. Flesch *et al.* (2005) and Wang *et al.* (2008) compared the surface deformation field inferred from GPS data and Quaternary fault slip rate to mantle deformational fields inferred from *SKS*-wave splitting to interpret a strong coupling between crust and mantle beneath Tibet. Waveform modeling of receiver functions by Sherrington *et al.* (2004), however, detected

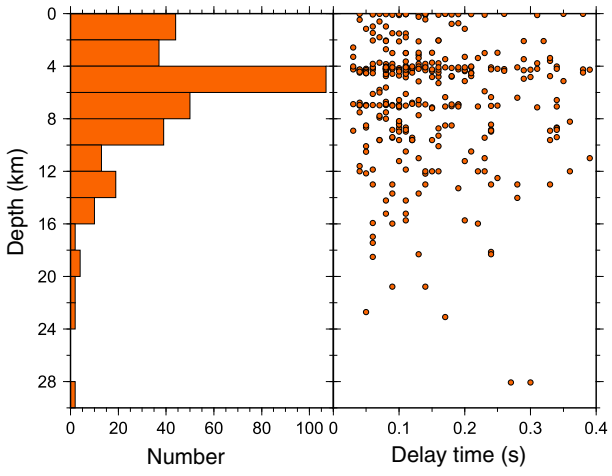

Figure 8. Depth distribution of earthquakes analyzed in this study, showing a predominance of events at depths less than 16 km (left) and no clear dependence of δt on depth (right). The color version of this figure is available only in the electronic edition.

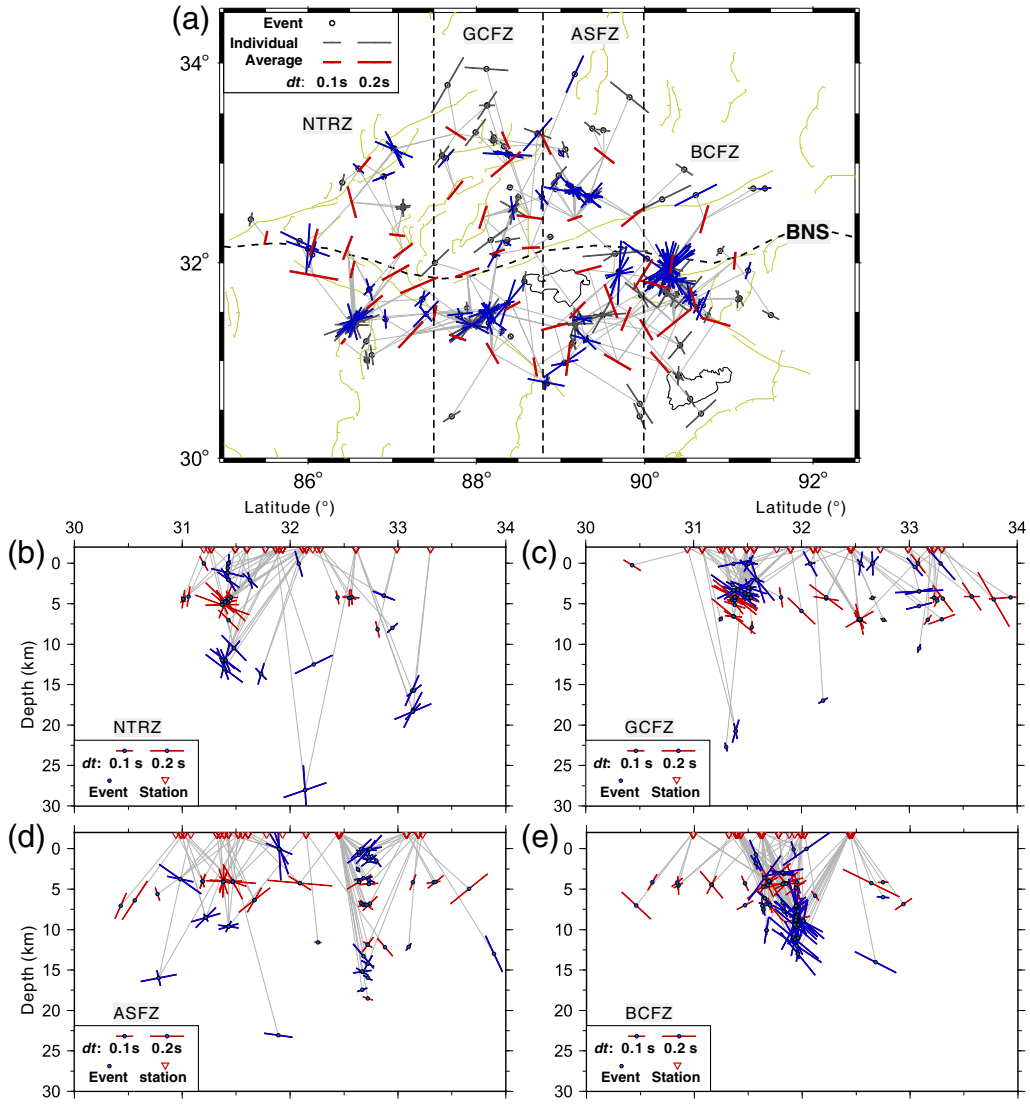

Figure 9. (a) Individual splitting parameters assigned to earthquake epicenters (blue bars with depth error less than 3 km and gray bars with depth error larger than 3 km) together with the respective average results (red bars) at stations. Gray thin lines connect epicentral locations with stations. The study region is divided into four zones, named the Nyima-Tingri rift zone (NTRZ), Gyaring Co fault zone (GCFZ), Amdo-Sewa fault zone (ASFZ), and Beng Co fault zone (BCFZ), according to surface structures that concentrate seismicity. Plots (b–e) correspond to the aforementioned zones: they show individual anisotropy parameters projected on vertical planes along a north–south direction (blue bars for events with depth error less than 3 km and red bars with depth error larger than 3 km). Gray thin lines connect sources and stations installed on the surface (inverted red triangles). Scales for delay time are included in corner boxes. The color version of this figure is available only in the electronic edition.

different anisotropic layers within the crust. The relatively weak middle or lower crust exhibited flow, indicating decoupling between crust and mantle. Peng *et al.* (2017) and Hu *et al.* (2018) recently reported further seismological evidence for lower crustal flow in southeastern areas of the Tibetan margin. The deformation style in central Tibet remains uncertain, due to sparse data coverage and limited research on upper-crustal anisotropy. Figure 11 compares SWS results obtained by this study to *SKS*-wave splitting obtained by other studies. Fast *SKS*-wave directions assume a primarily east-northeast–west-southwest strike (McNamara *et al.*, 1994; Sandvol *et al.*, 1997; Huang *et al.*, 2000; Chen, Martin, *et al.*, 2010; Zhao *et al.*, 2014; Chen *et al.*, 2015) and clearly show the bias of upper-mantle anisotropy. Fast polarization directions from upper-crustal anisotropy detected by this study do not show a consistent trend and clearly differ from fast *SKS*-wave polarization directions. The average misfit angle between our results and the nearest fast *SKS*-wave directions was 43°. This clearly suggests mechanical decoupling between the upper crust and upper mantle.

When compared with the 0.83 ± 0.35 s delay time obtained by the *Pms*-wave splitting study in western Tibet (Wu *et al.*, 2015), the average 0.15 ± 0.01 s delay time observed for the central Tibetan upper crust suggests that this domain represents a small part of the anisotropy of the entire crust. Crustal anisotropy may thus originate in the

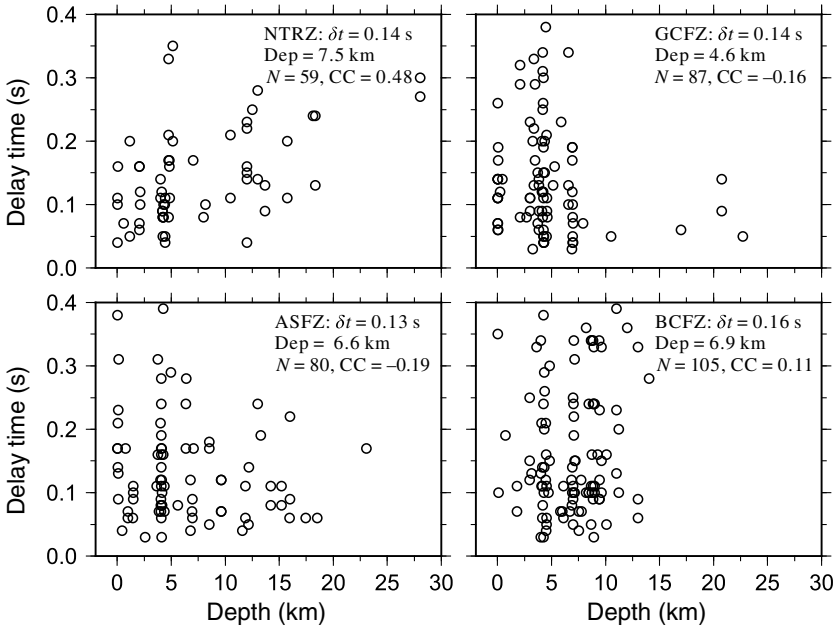

Figure 10. Delay time versus focal depth at the four zones delimited in Figure 9. The upper right quadrant of each panel describes the region name, average value of δt, mean depth of analyzed earthquakes (Dep), total number of events (N), and correlation coefficient (CC) between delay time δt and event depth.

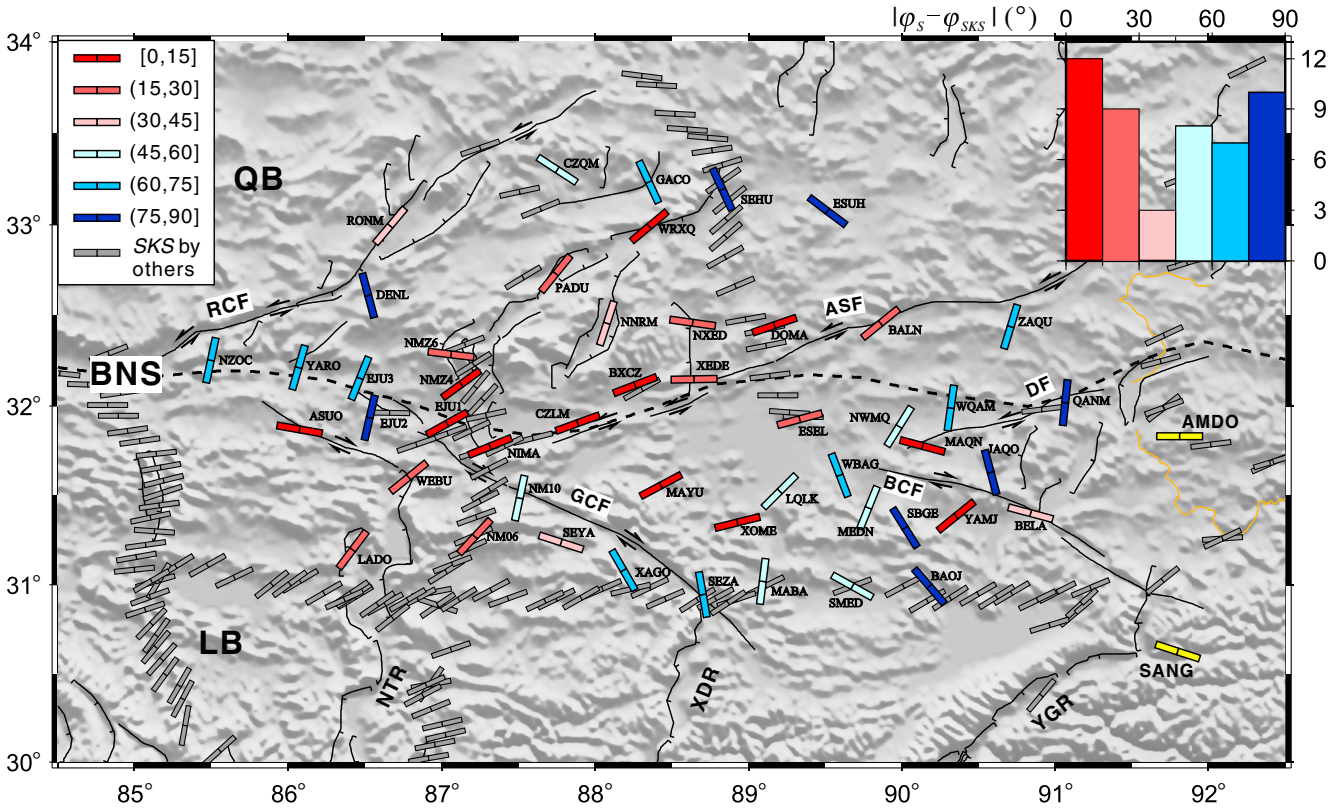

Figure 11. Crustal anisotropy compared with *SKS*-splitting fast directions. We use six colors to represent angle difference $|\varphi_S - \varphi_{SKS}|$ between fast direction determined in this study φ_S and *SKS*-splitting fast direction φ_{SKS} at the nearest station (legends, degrees). (Inset) Statistical distribution of the aforementioned difference also with the same colors. Gray bars represent *SKS*-splitting fast directions calculated by previous studies (McNamara *et al.*, 1994; Sandvol *et al.*, 1997; Huang *et al.*, 2000; Chen, Martin, *et al.*, 2010; Chen *et al.*, 2015; Zhao *et al.*, 2014). Yellow bars present fast directions of the middle-lower crustal anisotropy around Stations AMDO and SANG (Sherrington *et al.*, 2004). Abbreviations are the same as Figure 1. The color version of this figure is available only in the electronic edition.

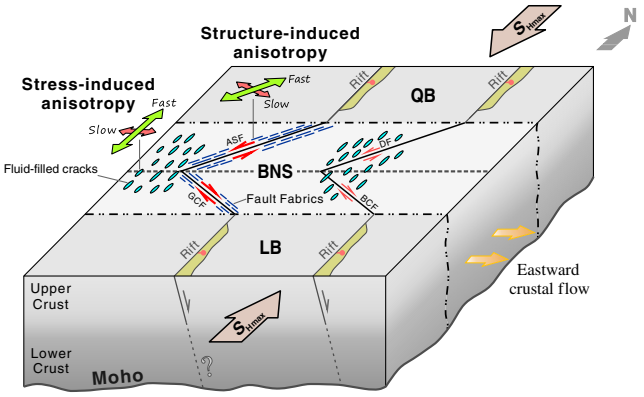

Figure 12. Cartoon to help the interpretation of the upper-crustal anisotropy in central Tibet. The anisotropy in the eastern and western parts agrees well with the fluid-filled cracks parallel to maximum horizontal compressive stress az$S_{H\,max}$. It is therefore considered as stress-induced anisotropy. Stations near active conjugate strike-slip faults show fast directions parallel to the fault fabrics, which means structural anisotropy. In addition, eastward middle-lower crustal flow causes the basal shear necessary for formation of conjugate strike-slip faults. Abbreviations are the same as Figure 1. The color version of this figure is available only in the electronic edition.

middle-lower crust, as suggested for the eastern margin of Tibet by Chen *et al.* (2013). Crustal structures with low *S*-wave velocity (Rapine *et al.*, 2003), high conductivity (Solon *et al.*, 2005), and lacking seismicity deeper than 30 km (Langin *et al.*, 2003; Zhu *et al.*, 2017) further indicate a ductile and even partially melted middle-lower crust. This could explain the strong crustal seismic attenuation observed from nearby areas (Zhao *et al.*, 2013). Middle-lower crustal flow may be ongoing (Klemperer, 2006) and thus able to induce the decoupled deformation between the upper crust and upper mantle. The east–west-oriented middle-lower crustal anisotropy observed from Stations SANG and AMDO supports the interpretation of east–west middle-lower crustal flow in central Tibet (Sherrington *et al.*, 2004). We therefore infer that conjugate faults are not lithospheric-scale faults and only affect the upper crust. Under conditions of north–south contraction, the basal shearing that induces the formation of conjugate faults originates from the influence of eastward middle-lower crustal flow on the base of the upper crust (Fig. 12) and not from asthenospheric flow acting on the base of the mantle lithosphere (Yin and Taylor, 2011). Further research using *Pms*-splitting-based imaging of crustal anisotropy and body-wave and surface-wave tomography of velocity structures can help confirm these inferences and increase understanding of regional deformation.

Conclusions

The present study interpreted 331 SWS vectors (fast wave polarization direction and delay time) obtained from 194 seismic events, mostly occurring at depths less than 20 km and recorded by 49 stations deployed as part of the SANDWICH project. Estimated splitting parameters revealed anisotropy in the upper crust of central Tibet. The mean delay times ranged from 0.04 ± 0.10 s to 0.29 ± 0.03 s, with an average value of 0.15 ± 0.01 s. Delay time did not clearly depend on increasing event depth. Fast-wave polarization directions at stations located in eastern and western zones of the study area were consistent with the north-northeast orientation of maximum horizontal compressive stress. Stations near the active conjugate strike-slip faults show fast directions generally parallel to the strikes of faults. Inactive thrust faults representing the Cretaceous–Tertiary shortening of central Tibet also clearly influenced anisotropy detected by nearby stations. This complex pattern demonstrates that both the local structures and stress fields influence SWS parameters (Fig. 12).

Most fast polarization directions obtained here differ from fast *SKS*-wave polarization directions reported by previous studies. The average misfit angle of 43° between our results and fast *SKS*-wave directions indicates decoupled deformation between the upper crust and upper mantle in central Tibet. The average 0.15 s delay time for the upper crust represents only a small part of the anisotropy for the entire crust (relative to delay times obtained by *Pms*-wave splitting for nearby areas). We therefore conclude that the crustal anisotropy probably arises in the middle-lower crust.

Crustal structures with low *S*-wave velocity, lack of seismicity deeper than 30 km, and east–west fast directions in the middle-lower crust all indicate a ductile and even partially melted middle-lower crust. Continuous flow in the middle-lower crust likely causes decoupled deformation between the upper crust and upper mantle. Conjugate faults are not lithospheric-scale faults and only penetrate the upper crust. In summary, continental deformation in central Tibet is governed by eastward ductile middle-lower crustal flow that causes the basal shear necessary for formation of conjugate strike-slip faults (Fig. 12).

Data and Resources

The earthquake mechanisms in this study region were extracted from the Global Centroid Moment Tensor Project database https://www.globalcmt.org/CMTsearch.html (last accessed May 2018). The stress direction shown in the inset of Figure 1 was obtained from http://www.world-stress-map.org (last accessed August 2016). The *SKS*-splitting measurements shown in Figure 11 were searched using http://splitting.gm.univ-montp2.fr/ (last accessed January 2018). The stress inversion was made using the MSATSI package (Martínez-Garzón *et al.*, 2014) downloaded from https://www.induced.pl/msatsi (last accessed May 2018).

Acknowledgments

This article is dedicated to the memory of Zhongjie Zhang (1964–2013).

The authors thank the Seismic Array Laboratory, Institute of Geology and Geophysics, Chinese Academy of Sciences for the preparation and maintenance of recording instruments. The authors appreciate the assistance of the members of the SANDWICH field team, who collected the data used in this study, including Wei Li, Yaohui Duan, Minghui

Zhang, Xi Guo, Beibei Zhou, Shitan Nie, Gaochun Wang, Sicheng Zuo, Zhen Liu, Zhenbo Wu, Minling Wang, Ping Tan, and Xiaopeng Zhou. Helpful comments and suggestions from Martha Savage and three anonymous reviewers greatly improved this article. The authors gratefully acknowledge financial support for this research from the National Key Research and Development Program of China (Grant Numbers 2016YFC0600301 and 2016YFC0600302), the Second Tibetan Plateau Scientific Expedition and Research Program (STEP) (Grant Number 2019QZKK0701), and the National Natural Science Foundation of China (Grant Numbers 41804058, 41674064, 41704042, 41574082, 41522401, 41474068, and 41574056).

References

Armijo, R., P. Tapponnier, and H. Tonglin (1989). Late Cenozoic right-lateral strike-slip faulting in southern Tibet, *J. Geophys. Res.* **94,** no. B3, 2787–2838, doi: 10.1029/JB094iB03p02787.

Aster, R. C., P. M. Shearer, and J. Berger (1990). Quantitative measurements of shear wave polarizations at the Anza seismic network, southern California: Implications for shear wave splitting and earthquake prediction, *J. Geophys. Res.* **85,** no. B8, 12,449–12,473, doi: 10.1029/JB095iB08p12449.

Boness, N. L., and M. D. Zoback (2004). Stress-induced seismic velocity anisotropy and physical properties of the SAFOD Pilot Hole in Parkfield, CA, *Geophys. Res. Lett.* **31,** L15S17, doi: 10.1029/2003GL019020.

Boness, N. L., and M. D. Zoback (2006). Mapping stress and structurally controlled crustal shear velocity anisotropy in California, *Geology* **34,** no. 10, 825–828, doi: 10.1130/g22309.1.

Booth, D. C., and S. Crampin (1985). Shear-wave polarizations on a curved wave-front at an isotropic free-surface, *Geophys. J. Roy. Astron. Soc.* **83,** no. 1, 31–45, doi: 10.1111/j.1365-246X.1985.tb05154.x.

Burg, J. P., P. Davy, and J. Martinod (1994). Shortening of analog models of the continental lithosphere—New hypothesis for the formation of the Tibetan plateau, *Tectonics* **13,** no. 2, 475–483, doi: 10.1029/93tc02738.

Chen, Q. Z., J. T. Freymueller, Q. Wang, Z. Q. Yang, C. J. Xu, and J. N. Liu (2004). A deforming block model for the present-day tectonics of Tibet, *J. Geophys. Res.* **109,** no. B1, doi: 10.1029/2002jb002151.

Chen, W.-P., and S. Ozalaybey (1998). Correlation between seismic anisotropy and Bouguer gravity anomalies in Tibet and its implications for lithospheric structures, *Geophys. J. Int.* **135,** no. 1, 93–101, doi: 10.1046/j.1365-246X.1998.00611.x.

Chen, W.-P., M. Martin, T. L. Tseng, R. L. Nowack, S. H. Hung, and B. S. Huang (2010). Shear-wave birefringence and current configuration of converging lithosphere under Tibet, *Earth Planet. Sci. Lett.* **295,** nos. 1/2, 297–304, doi: 10.1016/j.epsl.2010.04.017.

Chen, Y., J. Badal, and J. F. Hu (2010). Love and Rayleigh wave tomography of the Qinghai-Tibet plateau and surrounding areas, *Pure. Appl. Geophys.* **167,** no. 10, 1171–1203, doi: 10.1007/s00024-009-0040-1.

Chen, Y., W. Li, X. Yuan, J. H. Badal, and J. W. Teng (2015). Tearing of the Indian lithospheric slab beneath southern Tibet revealed by SKS-wave splitting measurements, *Earth Planet. Sci. Lett.* **413,** 13–24, doi: 10.1016/j.epsl.2014.12.041.

Chen, Y., Z. J. Zhang, C. Q. Sun, and J. Badal (2013). Crustal anisotropy from Moho converted Ps wave splitting analysis and geodynamic implications beneath the eastern margin of Tibet and surrounding regions, *Gondwana Res.* **24,** nos. 3/4, 946–957, doi: 10.1016/j.gr.2012.04.003.

Clark, M. K., and L. H. Royden (2000). Topographic ooze: Building the eastern margin of Tibet by lower crustal flow, *Geology* **28,** no. 8, 703–706, doi: 10.1130/0091-7613(2000)28<703:tobtem>2.0.co;2.

Cochran, E. S., and K. A. Kroll (2015). Stress- and structure-controlled anisotropy in a region of complex faulting—Yuha Desert, California, *Geophys. J. Int.* **202,** 1109–1121, doi: 10.1093/gji/ggv191.

Cochran, E. S., Y.-G. Li, and J. E. Vidale (2006). Anisotropy in the shallow crust observed around the San Andreas fault before and after the 2004 M 6.0 Parkfield earthquake, *Bull. Seismol. Soc. Am.* **96,** no. 4B, S364–S375, doi: 10.1785/0120050804.

Cochran, E. S., J. E. Vidale, and Y.-G. Li (2003). Near-fault anisotropy following the Hector Mine earthquake, *J. Geophys. Res.* **108,** no. B9, 2436, doi: 10.1029/2002JB002352.

Crampin, S., D. Bamford, and R. W. McGonigle (1978). Estimating crack parameters by inversion of P-wave velocity-anisotropy, *Geophys. J. Roy. Astron. Soc.* **53,** no. 1, 173.

England, P., and G. Houseman (1986). Finite strain calculations of continental deformation: 2. Comparison with the India–Asia collision zone, *J. Geophys. Res.* **91,** no. B3, 3664–3676, doi: 10.1029/JB091iB03p03664.

England, P., and D. McKenzie (1982). A thin viscous sheet model for continental deformation, *Geophys. J. Roy. Astron. Soc.* **70,** no. 2, 295–321, doi: 10.1111/j.1365-246X.1982.tb04969.x.

Flesch, L. M., W. E. Holt, P. G. Silver, M. Stephenson, C. Y. Wang, and W. W. Chan (2005). Constraining the extent of crust–mantle coupling in central Asia using GPS, geologic, and shear wave splitting data, *Earth Planet. Sci. Lett.* **238,** nos. 1/2, 248–268, doi: 10.1016/j.epsl.2005.06.023.

Fu, Y. V., Y. J. Chen, A. Li, S. Zhou, X. Liang, G. Ye, G. Jin, M. Jiang, and J. Ning (2008). Indian mantle corner flow at southern Tibet revealed by shear wave splitting measurements, *Geophys. Res. Lett.* **35,** L02308, doi: 10.1029/2007gl031753.

Gan, W., P. Zhang, Z.-K. Shen, Z. Niu, M. Wang, Y. Wan, D. Zhou, and J. Cheng (2007). Present-day crustal motion within the Tibetan Plateau inferred from GPS measurements, *J. Geophys. Res.* **112,** no. B8, doi: 10.1029/2005jb004120.

Gao, Y., J. Wu, Y. S. Fukao, Y. T. Shi, and A. L. Zhu (2011). Shear wave splitting in the crust in North China: Stress, faults and tectonic implications, *Geophys. J. Int.* **187,** no. 2, 642–654, doi: 10.1111/j.1365-246X.2011.05200.x.

Garthwaite, M. C., H. Wang, and T. J. Wright (2013). Broadscale interseismic deformation and fault slip rates in the central Tibetan Plateau observed using InSAR, *J. Geophys. Res.* **118,** no. 9, 5071–5083, doi: 10.1002/jgrb.50348.

Guo, G. H., Z. Zhang, J. W. Cheng, Z. P. Dong, J. P. Yan, and Y. W. Ma (2015). Seismic anisotropy in the crust in northeast margin of Tibetan Plateau and tectonic implication, *Chin. J. Geophys.* **58,** no. 11, 4092–4105, doi: 10.6038/cjg20151117 (in Chinese with English abstract).

Hu, J. F., J. Badal, H. Y. Yang, G. Q. Li, and H. C. Peng (2018). Comprehensive crustal structure and seismological evidence for lower crustal flow in the southeastern margin of Tibet revealed by receiver functions, *Gondwana Res.* **55,** 42–59, doi: 10.1016/j.gr.2017.11.007.

Huang, W. C., J. F. Ni, F. Tilmann, D. Nelson, J. R. Guo, W. J. Zhao, J. Mechie, R. Kind, J. Saul, R. Rapine, *et al.* (2000). Seismic polarization anisotropy beneath the central Tibetan Plateau, *J. Geophys. Res.* **105,** no. B12, 27,979–27,989, doi: 10.1029/2000jb900339.

Johnson, J. H., M. K. Savage, and J. Townend (2011). Distinguishing between stress-induced and structural anisotropy at Mount Ruapehu volcano, New Zealand, *J. Geophys. Res.* **116,** no. B12303, doi: 10.1029/2011JB008308.

Kapp, P., M. A. Murphy, A. Yin, T. M. Harrison, L. Ding, and J. H. Guo (2003). Mesozoic and Cenozoic tectonic evolution of the Shiquanhe area of western Tibet, *Tectonics* **22,** no. 4, 1029, doi: 10.1029/2001tc001332.

Kapp, P., A. Yin, T. M. Harrison, and L. Ding (2005). Cretaceous-Tertiary shortening, basin development, and volcanism in central Tibet, *Geol. Soc. Am. Bull.* **117,** nos. 7/8, 865–878, doi: 10.1130/b25595.1.

Kapp, P., A. Yin, C. E. Manning, T. M. Harrison, M. H. Taylor, and L. Ding (2003). Tectonic evolution of the early Mesozoic blueschist-bearing Qiangtang metamorphic belt, central Tibet, *Tectonics* **22,** no. 4, 1043, doi: 10.1029/2002tc001383.

Kapp, P., A. Yin, C. E. Manning, M. Murphy, T. M. Harrison, M. Spurlin, D. Lin, X. G. Deng, and C. M. Wu (2000). Blueschist-bearing metamorphic core complexes in the Qiangtang block reveal deep crustal structure of northern Tibet, *Geology* **28,** no. 1, 19–22.

Kern, H., and H.-R. Wenk (1990). Fabric-related velocity anisotropy and shear wave splitting in rocks from the Santa Rosa Mylonite Zone, California, *J. Geophys. Res.* **95,** no. B7, 11,213–11,223, doi: 10.1029/JB095iB07p11213.

Kind, R., X. Yuan, J. Saul, D. Nelson, S. V. Sobolev, J. Mechie, W. Zhao, G. Kosarev, J. Ni, U. Achauer, *et al.* (2002). Seismic images of crust and upper mantle beneath Tibet: Evidence for Eurasian plate subduction, *Science* **298,** no. 5596, 1219–1221, doi: 10.1126/science.1078115.

Klemperer, S. L. (2006). Crustal flow in Tibet: Geophysical evidence for the physical state of Tibetan lithosphere, and inferred patterns of active flow, in *Channel Flow, Ductile Extrusion and Exhumation in Continental Collision Zones*, R. D. Law, M. P. Searle, and L. Godin (Editors), The Geological Society of London, London, United Kingdom, 39–70.

Ko, B., and H. Jung (2015). Crystal preferred orientation of an amphibole experimentally deformed by simple shear, *Nat. Comm.* **6,** doi: 10.1038/ncomms7586.

Langin, W. R., L. D. Brown, and E. A. Sandvol (2003). Seismicity of central Tibet from Project INDEPTH III seismic recordings, *Bull. Seismol. Soc. Am.* **93,** no. 5, 2146–2159, doi: 10.1785/0120030004.

Leary, P. C., S. Crampin, and T. V. McEvilly (1990). Seismic fracture anisotropy in the earths crust—An overview, *J. Geophys. Res.* **95,** no. B7, 11,105–11,114, doi: 10.1029/JB095iB07p11105.

Li, Z. F., and Z. G. Peng (2017). Stress- and structure-induced anisotropy in southern California from two decades of shear wave splitting measurements, *Geophys. Res. Lett.* **44,** no. 19, 9607–9614, doi: 10.1002/2017gl075163.

Li, Z. F., Z. G. Peng, Y. Ben-Zion, and F. L. Vernon (2015). Spatial variations of shear wave anisotropy near the San Jacinto fault zone in Southern California, *J. Geophys. Res.* **120,** 8334–8347, doi: 10.1002/2015JB012483.

Liang, X. F., X. B. Tian, G. H. Zhu, C. L. Wu, Y. H. Duan, W. Li, B. B. Zhou, M. H. Zhang, G. P. Yu, S. T. Nie, *et al.* (2016). SANDWICH: A 2D broadband seismic array in central Tibet, *Seismol. Res. Lett.* **87,** no. 4, 864–873, doi: 10.1785/0220150243.

Liu, G. C., X. F. Shang, R. Z. He, R. Gao, C. Q. Zou, and W. H. Li (2014). Topography of Moho beneath the central Qiangtang in North Tibet and its geodynamic implication, *Chin. J. Geophys.* **57,** no. 7, 2043–2053, doi: 10.6038/cjg20140702 (in Chinese with English abstract).

Liu, Y., T.-L. Teng, and Y. Ben-Zion (2004). Systematic analysis of shear-wave splitting in the aftershock zone of the 1999 Chi-Chi, Taiwan, earthquake: Shallow crustal anisotropy and lack of precursory variations, *Bull. Seismol. Soc. Am.* **94,** no. 6, 2330–2347.

Liu, Y., H. Zhang, C. Thurber, and S. Roecker (2008). Shear wave anisotropy in the crust around the San Andreas fault near Parkfield: Spatial and temporal analysis, *Geophys. J. Int.* **172,** 957–990, doi: 10.1111/j.1365-246X.2007.03618.x.

Lund, B., and J. Townend (2007). Calculating horizontal stress orientations with full or partial knowledge of the tectonic stress tensor, *Geophys. J. Int.* **170,** no. 3, 1328–1335, doi: 10.1111/j.1365-246X.2007.03468.x.

Martínez-Garzón, P., G. Kwiatek, M. Ickrath, and M. Bohnhoff (2014). MSATSI: A MATLAB package for stress inversion combining solid classic methodology, a new simplified user-handling, and a visualization tool, *Seismol. Res. Lett.* **85,** no. 4, 896–904, doi: 10.1785/0220130189.

McNamara, D. E., T. J. Owens, P. G. Silver, and F. T. Wu (1994). Shear-wave anisotropy beneath the Tibetan Plateau, *J. Geophys. Res.* **99,** no. B7, 13,655–13,665, doi: 10.1029/93jb03406.

Nascimento, A. F., F. H. R. Bezerra, and M. K. Takeya (2004). Dutile Precambrian fabric control of seismic anisotroy in the Açu dam area, northeastren Brazil, *J. Geophys. Res.* **109,** no. B10311, doi: 10.1029/2004JB003120.

Peng, H. C., H. Y. Yang, J. F. Hu, and J. Badal (2017). Three-dimensional S-velocity structure of the crust in the southeast margin of the Tibetan plateau and geodynamic implications, *J. Asian Earth Sci.* **148,** 210–222, doi: 10.1016/j.jseaes.2017.09.004.

Peng, Z. G., and Y. Ben-Zion (2004). Systematic analysis of crustal anisotropy along the Karadere–Düzce branch of the North Anatolian fault, *Geophys. J. Int.* **159,** no. 1, 253–274, doi: 10.1111/j.1365-246X.2004.02379.x.

Peng, Z. G., and Y. Ben-Zion (2005). Spatiotemporal variations of crustal anisotropy from similar events in the aftershocks of the 1999 M7.4 İzmit and M7.1 Düzce, Turkey, earthquake sequences, *Geophys. J. Int.* **160,** 1027–1043, doi: 10.1111/j.1365-246X.2005.02569.x.

Rapine, R., F. Tilmann, M. West, J. Ni, and A. Rodgers (2003). Crustal structure of northern and southern Tibet from surface wave dispersion analysis, *J. Geophys. Res.* **108,** no. B2, doi: 10.1029/2001jb000445.

Sandvol, E., J. Ni, R. Kind, and W. J. Zhao (1997). Seismic anisotropy beneath the southern Himalayas–Tibet collision zone, *J. Geophys. Res.* **102,** no. B8, 17,813–17,823, doi: 10.1029/97jb01424.

Savage, M. K. (1999). Seismic anisotropy and mantle deformation: What have we learned from shear wave splitting? *Rev. Geophys.* **37,** no. 1, 65–106, doi: 10.1029/98rg02075.

Savage, M. K., Y. Aoki, K. Unglert, T. Ohkura, K. Umakoshi, H. Shimizu, M. Iguchi, T. Tameguri, T. Ohminato, and J. Mori (2016). Stress, strain rate and anisotropy in Kyushu, Japan, *Earth Planet. Sci. Lett.* **439,** 129–142, doi: 10.1016/j.epsl.2016.01.005.

Savage, M. K., T. Ohminato, Y. Aoki, H. Tsuji, and S. M. Greve (2010). Stress magnitude and its temporal variation at Mt. Asama Volcano, Japan, from seismic anisotropy and GPS, *Earth Planet. Sci. Lett.* **290,** 403–414, doi: 10.1016/j.epsl.2009.12.037.

Savage, M. K., X. R. Shih, R. P. Meyer, and R. C. Aster (1989). Shear-wave anisotropy of active tectonic regions via automated *S*-wave polarization analysis, *Tectonophysics* **165,** nos. 1/4, 279–292, doi: 10.1016/0040-1951(89)90053-x.

Savage, M. K., A. Wessel, N. A. Teanby, and A. W. Hurst (2010). Automatic measurement of shear wave splitting and applications to time varying anisotropy at Mount Ruapehu volcano, New Zealand, *J. Geophys. Res.* **115,** no. B12321, doi: 10.1029/2010jb007722.

Sherrington, H. F., G. Zandt, and A. Frederiksen (2004). Crustal fabric in the Tibetan Plateau based on waveform inversions for seismic anisotropy parameters, *J. Geophys. Res.* **109,** no. B2, doi: 10.1029/2002jb002345.

Shi, X. H., E. Kirby, H. J. Lu, R. Robinson, K. P. Furlong, and E. Wang (2014). Holocene slip rate along the Gyaring Co fault, central Tibet, *Geophys. Res. Lett.* **41,** no. 16, 5829–5837, doi: 10.1002/2014gl060782.

Silver, P. G. (1996). Seismic anisotropy beneath the continents: Probing the depths of geology, *Annu. Rev. Earth Planet. Sci.* **24,** 385–432, doi: 10.1146/annurev.earth.24.1.385.

Silver, P. G., and W. W. Chan (1991). Shear wave splitting and subcontinental mantle deformation, *J. Geophys. Res.* **96,** no. B10, 16,429–16,454.

Solon, K. D., A. G. Jones, K. D. Nelson, M. J. Unsworth, W. F. Kidd, W. Wei, H. Tan, S. Jin, M. Deng, J. R. Booker, *et al.* (2005). Structure of the crust in the vicinity of the Banggong-Nujiang suture in central Tibet from INDEPTH magnetotelluric data, *J. Geophys. Res.* **110,** no. B10, doi: 10.1029/2003jb002405.

Sun, Y., F. L. Niu, H. F. Liu, Y. L. Chen, and J. X. Liu (2012). Crustal structure and deformation of the SE Tibetan plateau revealed by receiver function data, *Earth Planet. Sci. Lett.* **349,** 186–197, doi: 10.1016/j.epsl.2012.07.007.

Tadokoro, K., and M. Ando (2002). Evidence for rapid fault healing derived from temporal changes in S wave splitting, *Geophys. Res. Lett.* **29,** no. 4, 1047, doi: 10.1029/2001GL013644.

Tapponnier, P., G. Peltzer, A. Y. Ledain, R. Armijo, and P. Cobbold (1982). Propagating extrusion tectonics in Asia—New insights from simple experiments with plasticine, *Geology* **10,** no. 12, 611–616, doi: 10.1130/0091-7613(1982)10<611:petian>2.0.co;2.

Tapponnier, P., Z. Q. Xu, F. Roger, B. Meyer, N. Arnaud, G. Wittlinger, and J. S. Yang (2001). Geology—Oblique stepwise rise and growth of the Tibet plateau, *Science* **294,** no. 5547, 1671–1677, doi: 10.1126/science.105978.

Tatham, D. J., G. E. Lloyd, R. W. H. Butler, and M. Casey (2008). Amphibole and lower crustal seismic properties, *Earth Planet. Sci. Lett.* **267,** nos. 1/2, 118–128, doi: 10.1016/j.epsl.2007.11.042.

Taylor, M., and G. Peltzer (2006). Current slip rates on conjugate strike-slip faults in central Tibet using synthetic aperture radar interferometry, *J. Geophys. Res.* **111,** no. B12, doi: 10.1029/2005jb004014.

Taylor, M., A. Yin, F. J. Ryerson, P. Kapp, and L. Ding (2003). Conjugate strike-slip faulting along the Bangong-Nujiang suture zone accommodates coeval

east-west extension and north-south shortening in the interior of the Tibetan Plateau, *Tectonics* **22,** no. 4, 1044, doi: 10.1029/2002tc001361.

Teanby, N. A., J. M. Kendall, and M. Van der Baan (2004). Automation of shear-wave splitting measurements using cluster analysis, *Bull. Seismol. Soc. Am.* **94,** no. 2, 453–463, doi: 10.1785/0120030123.

Tian, X. B., Y. Chen, T. L. Tseng, S. L. Klemperer, H. Thybo, Z. Liu, T. Xu, X. F. Liang, Z. M. Bai, X. Zhang, *et al.* (2015). Weakly coupled lithospheric extension in southern Tibet, *Earth Planet. Sci. Lett.* **430,** 171–177, doi: 10.1016/j.epsl.2015.08.025.

Wang, C. Y., L. M. Flesch, P. G. Silver, L. J. Chang, and W. W. Chan (2008). Evidence for mechanically coupled lithosphere in central Asia and resulting implications, *Geology* **36,** no. 5, 363–366, doi: 10.1130/g24450a.1.

Wang, Q., F. L. Niu, Y. Gao, and Y. T. Chen (2016). Crustal structure and deformation beneath the NE margin of the Tibetan plateau constrained by teleseismic receiver function data, *Geophys. J. Int.* **204,** no. 1, 167–179, doi: 10.1093/gji/ggv420.

Wang, Q., P. Z. Zhang, J. T. Freymueller, R. Bilham, K. M. Larson, X. Lai, X. Z. You, Z. J. Niu, J. C. Wu, Y. X. Li, *et al.* (2001). Present-day crustal deformation in China constrained by global positioning system measurements, *Science* **294,** no. 5542, 574–577, doi: 10.1126/science.1063647.

Wu, C. L., X. B. Tian, T. Xu, X. F. Liang, Y. Chen, M. Taylor, J. Badal, Y. H. Duan, G. P. Yu, and J. W. Teng (2019). Deformation of crust and upper mantle in central Tibet caused by the northward subduction and slab tearing of the Indian lithosphere: New evidence based on shear wave splitting measurements, *Earth Planet. Sci. Lett.* **514,** 75–83.

Wu, J., Z. J. Zhang, F. S. Kong, B. B. Yang, Y. G. Yu, K. H. Liu, and S. S. Gao (2015). Complex seismic anisotropy beneath western Tibet and its geodynamic implications, *Earth Planet. Sci. Lett.* **413,** 167–175, doi: 10.1016/j.epsl.2015.01.002.

Wüstefeld, A., and G. Bokelmann (2007). Null detection in shear-wave splitting measurements, *Bull. Seismol. Soc. Am.* **97,** no. 4, 1204–1211.

Yang, Z., A. Sheehan, and P. Shearer (2011). Stress-induced upper crustal anisotropy in southern California, *J. Geophys. Res.* **116,** no. B02302, doi: 10.1029/2010JB007655.

Yin, A. (2000). Mode of Cenozoic east-west extension in Tibet suggesting a common origin of rifts in Asia during the Indo-Asian collision, *J. Geophys. Res.* **105,** no. B9, 21,745–21,759, doi: 10.1029/2000jb900168.

Yin, A., and T. M. Harrison (2000). Geologic evolution of the Himalayan-Tibetan orogen, *Annu. Rev. Earth Planet. Sci.* **28,** 211–280, doi: 10.1146/annurev.earth.28.1.211.

Yin, A., and M. H. Taylor (2011). Mechanics of V-shaped conjugate strike-slip faults and the corresponding continuum mode of continental deformation, *Geol. Soc. Am. Bull.* **123,** nos. 9/10, 1798–1821, doi: 10.1130/b30159.1.

Zhang, P.-Z., Z. Shen, M. Wang, W. Gan, R. Bürgmann, P. Molnar, Q. Wang, Z. Niu, J. Sun, J. Wu, *et al.* (2004). Continuous deformation of the Tibetan Plateau from global positioning system data, *Geology* **32,** no. 9, 809–812, doi: 10.1130/g20554.1.

Zhang, S. Q., and S. Karato (1995). Lattice preferred orientation of olivine aggregates deformed in simple shear, *Nature* **375,** no. 6534, 774–777, doi: 10.1038/375774a0.

Zhang, X. M., J. W. Teng, R. M. Sun, F. Romanelli, Z. J. Zhang, and G. F. Panza (2014). Structural model of the lithosphere-asthenosphere system beneath the Qinghai-Tibet Plateau and its adjacent areas, *Tectonophysics* **634,** 208–226, doi: 10.1016/j.tecto.2014.08.017.

Zhang, Z., and S. Y. Schwartz (1994). Seismic anisotropy in the shallow crust of the Loma Prieta segment of the San Andreas fault system, *J. Geophys. Res.* **99,** no. 5, 9651–9661, doi: 10.1029/94JB00241.

Zhang, Z. J., and S. L. Klemperer (2005). West-east variation in crustal thickness in northern Lhasa block, central Tibet, from deep seismic sounding data, *J. Geophys. Res.* **110,** no. B9, doi: 10.1029/2004jb003139.

Zhao, J. M., D. Murodov, Y. Huang, Y. S. Sun, S. P. Pei, H. B. Liu, H. Zhang, Y. Y. Fu, W. Wang, H. G. Cheng, *et al.* (2014). Upper mantle deformation beneath central-southern Tibet revealed by shear wave splitting measurements, *Tectonophysics* **627,** 135–140, doi: 10.1016/j.tecto.2013.11.003.

Zhao, L. F., X. B. Xie, J. K. He, X. B. Tian, and Z. X. Yao (2013). Crustal flow pattern beneath the Tibetan Plateau constrained by regional *Lg*-wave *Q* tomography, *Earth Planet. Sci. Lett.* **383,** 113–122, doi: 10.1016/j.epsl.2013.09.038.

Zhou, B. B., X. F. Liang, G. Q. Lin, X. B. Tian, G. H. Zhu, J. Mechie, and J. W. Teng (2019). Upper crustal weak zone in central Tibet: An implication from three-dimensional seismic velocity and attenuation tomography results, *J. Geophys. Res.* **124,** 4654–4672, doi: 10.1029/2018JB016653.

Zhu, G. H., X. F. Liang, X. B. Tian, H. F. Yang, C. L. Wu, Y. H. Duan, W. Li, and B. B. Zhou (2017). Analysis of the seismicity in central Tibet based on the SANDWICH network and its tectonic implications, *Tectonophysics* **702,** 1–7, doi: 10.1016/j.tecto.2017.02.020.

Zinke, J. C., and M. D. Zoback (2000). Structure-related and stress-induced shear-wave velocity anisotropy: Observations from microearthquakes near the Calaveras fault in central California, *Bull. Seismol. Soc. Am.* **90,** no. 5, 1305–1312.

Chenglong Wu
Xiaobo Tian
Tao Xu
Xiaofeng Liang
Yun Chen
Zhiming Bai
Guiping Yu
Jiwen Teng
State Key laboratory of Lithospheric Evolution
Institute of Geology and Geophysics, Chinese Academy of Sciences
Beijing 100029, China
wuchenglong@mail.iggcas.ac.cn
txb@mail.iggcas.ac.cn
xutao@mail.iggcas.ac.cn
liangxf@mail.iggcas.ac.cn
yunchen@mail.iggcas.ac.cn
bbzzmm@mail.iggcas.ac.cn
yuguiping14@mail.iggcas.ac.cn
jwteng@mail.iggcas.ac.cn

Gaohua Zhu
Earth System Science Programme
Faculty of Science
Chinese University of Hong Kong
Sha Tin, Hong Kong 999077, China
zhugaohua@link.cuhk.edu.hk

José Badal
Physics of the Earth, Sciences B
University of Zaragoza
Pedro Cerbuna 12
50009 Zaragoza, Spain
badal@unizar.es

Manuscript received 18 December 2018;
Published Online 27 August 2019